Journal of Materials Chemistry A

Accepted Manuscript

ROYAL SOCIETY OF CHEMISTRY

www.rsc.org/materialsA

Oxygen transport pathways in Ruddlesden-Popper structured oxides revealed via in-situ neutron diffraction

Alex C. Tomkiewicz[a], Mazin Tamimi[a], Ashfia Huq[b], Steven McIntosh[a*]

[a] Department of Chemical and Biomolecular Engineering, Lehigh University, Bethlehem, PA 18016, USA
[b] Spallation Neutron Source, Oak ridge National Laboratory, Oak Ridge, TN 37830, USA

*Corresponding Author: Tel: 1-610-758-6835, Fax: 1-610-758-5057, email: mcintosh@lehigh.edu

Abstract

Ruddlesden-Popper structured oxides, general form $A_{n+1}B_nO_{3n+1}$, consist of n-layers of the perovskite structure stacked in between rock-salt layers, and have potential application in solid oxide electrochemical cells and ion transport membrane reactors. Three materials with constant Co/Fe ratio, $LaSrCo_{0.5}Fe_{0.5}O_{4-\delta}$ (n=1), $La_{0.3}Sr_{2.7}CoFeO_{7-\delta}$ (n=2), and $LaSr_3Co_{1.5}Fe_{1.5}O_{10-\delta}$ (n=3) were synthesized and studied via *in-situ* neutron powder diffraction between 765 K and 1070 K at a pO_2 of 10^{-1} atm. The structures were fit to a tetragonal P4/*mmm* space group, and were found to have increased total oxygen vacancy concentration in the order $La_{0.3}Sr_{2.7}CoFeO_{7-\delta}$ > $LaSr_3Co_{1.5}Fe_{1.5}O_{10-\delta}$ > $LaSrCo_{0.5}Fe_{0.5}O_{4-\delta}$, following the trend predicted for charge compensation upon increasing Sr^{2+}/La^{3+} ratio. The oxygen vacancies within the material were almost exclusively located within the perovskite layers for all of the crystal structures with only minimal vacancy formation in the rock-salt layer. Analysis of the concentration of these vacancies at each distinct crystallographic site and the anisotropic atomic displacement parameters for the oxygen sites reveals potential preferred oxygen transport pathways through the perovskite layers.

Introduction

Mixed ionic-electronic conducting (MIEC) oxides are of interest as candidate materials for solid oxide fuel cell (SOFC) cathodes and ion transport membranes (ITMs). SOFCs have long focused on efficient electrical energy production while ITMs find potential application in air separation and partial oxidation reactors. In both cases, high operating temperatures, typically exceeding 700 ^{o}C, are required to achieve facile surface kinetics and bulk ion transport. However, this high operating temperature shortens lifetime due to accelerated material degradation. An ongoing research goal is to develop MIEC materials with sufficient ionic conductivity to enable intermediate temperature operation between 500 ^{o}C and 700 ^{o}C[1,2].

One promising class of materials is the Ruddlesden-Popper family with general formula $A_{n+1}B_nO_{3n+1}$[2-9]. The Ruddlesden-Popper structure consists of n repeating layers of cubic perovskite alternating with rock salt layers, with n = ∞ corresponding to the cubic perovskite structure. These materials have been shown to possess high rates of ionic conductivity for O^{2-} anions. Transport mechanisms involving mobile oxygen interstitials have been shown to exist for Ruddlesden-Popper materials such as those with the composition Ln_2NiO_{4+d}[10-15], while other Ruddlesden-Popper structures exhibit the vacancy hopping mechanism similar to the cubic perovskites[16-19] The layered nature of the Ruddlesden-Popper structure can provide several different oxygen exchange pathways as compared to the single pathway available in the cubic perovskite, reducing the activation energy of oxygen transport and allowing higher rates at lower temperatures[17,20]. As such, Ruddlesden-Popper and other layered materials are seen as promising candidates for SOFC cathodes and ITMs[4,17,20,21]. Herein, we study a series of Ruddlesden-Popper structured materials, utilizing varying ratios of La/Sr in the A-site and Co/Fe in the B-site to form the n=1, n=2, and n=3 analogs with compositions $LaSrCo_{0.5}Fe_{0.5}O_{4-\delta}$ (RPn1), $La_{0.3}Sr_{2.7}CoFeO_{7-\delta}$ (RPn2), and $LaSr_3Co_{1.5}Fe_{1.5}O_{10-\delta}$ (RPn3), respectively. A visualization of the three Ruddlesden-Popper structures considered in this study is shown in Figure 1.

The ionic conductivity of oxygen deficient MIEC materials occurs through an oxygen vacancy hopping mechanism[22]. Thus the accurate determination of the concentration, location, and mobility of oxygen vacancies in the crystal lattice is essential to understand the ionic transport properties of these materials. An increase in mobile oxygen vacancies without significant structural changes corresponds to an increase in the rate of vacancy-mediated oxygen anion transport, with localization of these vacancies creating clear transport pathways through the materials[4] . This trend would not hold for oxygen interstitial mediated transport[9,11,13], for cases where pronounced sub-stoichiometry can lead to structural changes and/or vacancy ordering[23], or where the mobility of vacancies decreases within the same structure. The bulk ionic conductivities[16] and surface oxygen exchange rates[24] of the three Ruddlesden-Popper compositions have been measured previously, showing trends of RPn3 ≳RPn2 >> RPn1 and RPn2 ≳RPn3 >> RPn1 respectively. This work seeks to utilize *in-situ* neutron diffraction to identify oxygen exchange pathways within the materials and to link this with the ionic conductivity of each composition.

High temperature *in-situ* neutron powder diffraction can simultaneously determine detailed information about the crystal symmetry, lattice parameters, and atomic positions, occupancies, and displacement parameters of both the cations and anions in these materials[3,4,7,23-28]. Our group has previously demonstrated the efficacy of this technique for both cubic perovskite structured oxides[27,28] and layered perovskite structures[3,4]. The detailed information thus obtained allows prediction of the ionic transport pathways through these materials[3,4] and, in an increasing number of cases, the inferred ionic mobility has previously correlated directly with measured surface oxygen exchange rates[21,24,28].

Thermogravimetric analysis (TGA) is the most commonly utilized technique to determine the oxygen stoichiometry of these materials; however, TGA can be problematic in terms of ensuring sample equilibrium and accurate knowledge of a reference oxidation state from which to calculate all other values. This can lead to significant variation in reported values of oxygen stoichiometry for the same material [25,27,28]. While there can be issues related to the correlation between the oxygen stoichiometry and anisotropic nuclear densities determined via Rietveld refinement of the neutron diffraction data, there are no issues with reference states. Furthermore, it is important to note that each diffraction data set, that is each composition at each temperature, is analyzed completely independently of all others. Neutron diffraction also allows for the occupancy of each oxygen site to be refined separately, showing localization of vacancy formation, providing a significant advantage over alternative techniques.

Each Rietveld refinement starts with default values with only instrument parameters, crystal symmetry, and atomic positions manually entered. From there, each refinement refines all parameters independently of all other refinements. The reported values and trends in oxygen stoichiometry (decreasing with increasing temperature and decreasing pO_2) and anisotropic or isotropic nuclear density (increasing with increasing temperature and decreasing occupancy) are only compared at the end of all refinements and serve as a check on the relative accuracy of the refinements. Additional checks for accuracy include similar occupancy determination for the same, or very similar, materials by different research teams utilizing different diffractometers and sample environment systems [26,27,29], and correlation between structure controlled and diffraction determined oxygen stoichiometry. This second check is clearly demonstrated in the accurate determination that the perovskite $SrCo_{0.8}Fe_{0.2}O_{2.5}$ is formed from disordering of the Brownmillerite structured $Sr_2Co_{1.6}Fe_{0.4}O_5$ phase[23]

Experimental

Synthesis of phase pure samples of n=1, n=2, and n=3 Ruddlesden-Popper phases with identical La/Sr and Co/Fe ratios was not feasible due to phase instability. Attempts to synthesize these materials yielded a mixture of Ruddlesden-Popper, perovskite, and simple oxide phases. Materials with identical Co/Fe ratios but varying La/Sr ratios were synthesized based on similar compositions reported in the literature[16,30]. A tolerance factor for the n = 1 Ruddlesden-Popper phases can be calculated based on the work of Sharma and Singh[31]. Compositions were chosen to achieve n=1 tolerance factors of approximately 1.08, corresponding to a tetragonal *T* phase K_2NiF_4-type structure. $LaSrCo_{0.5}Fe_{0.5}O_{4-\delta}$ (RPn1), $La_{0.3}Sr_{2.7}CoFeO_{7-\delta}$ (RPn2), and $LaSr_3Co_{1.5}Fe_{1.5}O_{10-\delta}$ (RPn3) were synthesized as single phases with only minor presence of single perovskite impurity phases.

All materials were synthesized using metal nitrate solutions in a modified Pechini method, as described previously[32]. $La(NO_3)_3$ [99.9%, Alfa Aesar, Ward Hill, MA, USA], $Sr(NO_3)_2$ [99.9%, Alfa Aesar], $Co(NO_3)_2$ [98.0-102.0%, Alfa Aesar], and $Fe(NO_3)_2$ [98.0-102.0%, Alfa Aesar] nitrate powders were dissolved in distilled water and subsequently titrated using an EDTA titrant [0.100 M, Ricca Chemical, Arlington, TX, USA]. The Ruddlesden-Popper phases were synthesized from a stoichiometric mixture of metal nitrate solutions in combination with EDTA [Alfa Aesar, 99%] and citric acid [Alfa Aesar, 99+%] as complexing agents. Excess water was evaporated from this solution to form a gel which was then combusted in air at 573 K for 12 hours. The resulting cake was then ground into powder and then calcined in air at 1623 K

for 10 hours. The finalized powder samples were characterized by X-ray diffraction [Rigaku Miniflex II, Texas, USA] to verify phase purity.

Neutron diffraction measurements were conducted at the POWGEN beamline, Spallation Neutron Source (SNS), Oak Ridge Laboratory, Oak Ridge, TN, USA. Powder samples were placed in a quartz sample holder which was suspended within the neutron beam with an experimental system described previously[4]. The furnace temperature was calibrated using a ZnO reference sample[33]. Powder samples were equilibrated under a continuous flow of an ultra-high purity mixture of O_2 and N_2 with a pO_2 of 10^{-1} atm at 500 sccm for a period of at least one hour prior to measurement at each temperature. Diffraction patterns were collected at 1070 K, 967 K, 865 K, and 765 K in the d-spacing range of 0.45 – 5.35 Å until a total accelerator source proton charge of 9.0 x 10^{12} pC (~2 hour measuring time) was reached. Several patterns with shortened collection times (7.50 x 10^{11} pC) were collected and examined prior to the 2 hour measurement to ensure that the sample had reached equilibrium, monitored via shift in lattice parameter. Samples were declared equilibrated after there was no observed change in the collected patterns for at least 3 collection periods.

Rietveld[34] refinements were performed on the diffraction patterns using the GSAS package[35] with the EXPGUI interface[36]. Background scans of the quartz sample holder were subtracted from the raw data, with remaining background modeled by a shifted Chebyschev function. The profile was modeled using an extended form of the profile function originally derived by Von Dreele, Jorgensen, and Windsor[37] to account for Lorentzian broadening. The lattice parameters, fractional occupancy of all oxygen sites, atomic displacement parameters and positions for each atom, and profile parameters (γ_1, σ_1 and σ_2), were all independently refined for each data set. DIFA, absorption, and scaling parameters were constrained across the measured temperatures for each sample as these should not vary with sample temperature. Decisions regarding which parameters to refine, for example whether atomic displacement should be isotropic or anisotropic, were made with regard to significant changes in the cumulative χ^2 value.

It should be noted that for the RPn2 and RPn3 structures, the multiple A-sites within the unit cell could allow for the A-site in the rock salt to have a different composition from the stoichiometric ratio. Furthermore, the similar coherent neutron scattering lengths of La and Sr, at 8.24 and 7.02 respectively, make it difficult to distinguish between the two in neutron diffraction experiments. Attempts to refine the site occupancy for the multiple A-sites from the neutron diffraction patterns yielded results showing that all sites had similar compositions within standard deviation, and thus the ratios of the cations composing the A-sites were fixed at the stoichiometric ratios. Refinement of the La/Sr ratio using synchrotron X-ray data was unsuccessful due to the formation of additional phases at room temperature.

Results

Neutron diffraction patterns were collected for the three prepared Ruddlesden-Popper phases, Figure 2. All three samples were fit to a tetragonal structure, space group *I4/mmm*. Less than 4 wt-% of a cubic perovskite impurity (space group $Pm\bar{3}m$) was identified in each sample, with positions denoted by an asterisk in Figure 2. Refined values of all parameters and χ^2 for neutron data collected at 1070 K for all three phases are shown in Tables 1-3. The same parameters were refined at each temperature. The fit quality was not improved for any of the materials either by ordering of the A-sites and/or the B-sites or by allowing significant deviations in overall composition from the as-synthesized target values. The

cation occupancies at each site were therefore fixed to their stoichiometric ratios. No evidence of a phase change was identified in any of the Ruddlesden-Popper structures examined between 765 K and 1070 K. All refined crystallographic parameters for each material are provided in Tables S1, S2 and S3.

The *a* and *c* lattice parameters as a function of temperature for all three samples are shown in Figures 3 and 4, respectively. The RPn2 phase has the largest *a*-axis lattice parameter, followed by the RPn3 and RPn1 samples. This is the expected trend based on the variation of average cation radius between these phases, with substitution of the larger Sr^{2+} cation for La^{3+} resulting in a larger *a* parameter. The average B-site cation oxidation state, and therefore B-site ionic radii, will also influence the lattice parameters. The calculated average B-site oxidation states vary in the ranges 3.0-2.64, 3.38-3.12, and 3.67-3.08 from 500-800 ^{o}C for the RPn1, RPn2, and RPn3 phases, respectively.

The simultaneously varying Ruddlesden-Popper structures, A-site ratios, and oxygen stoichiometries make it difficult to deconvolute the impact of each parameter on the lattice parameter. Previous research has shown that for an n=1 material of similar composition, the *a* lattice parameter is less responsive to temperature change than the *c* lattice, as the *c* axis expansion is less restricted by the expansion of the rock-salt layers[38]. Out of the materials examined, the n=1 and n=3 structures follow this trend identically, however the n=2 phase shows a greater expansion along the *a* axis than along the *c* axis. This is expected to be due to the conflicting thermal and chemical expansion along the *c* axis, as while thermal expansion occurs with increasing temperature, the presence of the heavily vacant O3 site of the n=2 structure causes a compression of the center perovskite cell with increasing temperature, evidenced by a shift of the Co1/Fe1 site towards the center of the unit cell. This is shown in the atomic positions on the supplementary Tables S1, S2, and S3. This decreases the expansion that may be expected along the *c* axis, while having little effect on the *a* lattice expansion. A similar effect was previously observed for PBCO and NBCO perovskite materials[3,4].

Fourier density maps were generated with GSAS for each of the three samples at 1070 K to gain information about the motion and preferred oxygen transport pathways within the materials, Figures 5-7. These figures show the observed nuclear density at both metal cations and anionic oxygen sites within the Ruddlesden-Popper unit cell. The progression of color from blue to green to red denotes an increase in the observed nuclear density, showing the probable positions of the atoms. The three figures represent isosurface levels of 0.45, 0.4, and 0.555, corresponding to 3.8%, 4.2%, and 5.3% of the maximum density, respectively. Figures showing lower isosurface levels are included in the supplementary materials, Figures S1, S2, and S3.

No evidence for oxygen interstitials was observed for any of the materials, evidenced by the lack of nuclear density outside of the expected crystallographic sites. Ruddlesden-Popper phases with compositions such as $La_2NiO_{4+\delta}$ have been shown to contain oxygen interstitials as part of an interstitial mediated oxygen transport mechanism[9]. As with related neutron diffraction studies, we find no evidence for the existence of oxygen interstitials within an oxygen deficient material[39].

The oxygen sites within $LaSrCo_{0.5}Fe_{0.5}O_{4-\delta}$ (RPn1), Figure 5, were found to be close to fully occupied below 967 K; oxygen occupancies refined to values within a standard deviation of 1.0 were therefore held constant at full occupancy, Figure 8a. The first measureable vacancies are located at the O2 site, the equatorial site in the perovskite layer, at 967 K. The O1 site, located in the rock-salt layer, was found to be fully occupied until 1070 K where an oxygen occupancy of 0.974(8), slightly outside of the standard deviation from 1.0, was determined. These results are in line with previous findings on related Ruddlesden-Popper structures[38,40]. The atomic displacement parameters for the oxygen atoms were

best fit with an anisotropic model, Table 1, with preferential displacement perpendicular to the central B-site of the perovskite octahedron. For the O1 site at 1070K, $U_{11}=U_{22}>2U_{33}$; for the O2 site, $U_{33}>1.25U_{22}\sim3U_{11}$. These distortions in local nuclear density are illustrated as the observed non-spherical nuclear density in the Fourier map, Figure 5, and are apparent as weak signals in the nuclear density map, Figure S1.

In contrast, the $La_{0.3}Sr_{2.7}CoFeO_{7-\delta}$ (RPn2) refinement, Figure 6, showed significant deviations from full oxygen occupancy, i.e. the presence of oxygen vacancies, at all measured temperatures. These vacancies were formed primarily in the O3 position in the center of the perovskite layer, Figure 8b. Refined occupancies for this site ranged from 0.71(1) at 765 K to 0.56(2) at 1070 K. Smaller vacancy concentrations occurred in the neighboring O2 site, while the O1 site that borders the rock-salt layer remained fully occupied at all measured temperatures. The O2 oxygen position was best fit by an anisotropic model for atomic displacement, with preferred displacement towards the O2 site, Table 2. The O3 and O1 positions were fit equally well with either an isotropic or anisotropic atomic displacement model and were thus set as isotropic.

The corresponding Fourier nuclear density map, Figure 6, shows low nuclear density around the O3 position, as expected based on the low occupancy of this oxygen site. The nuclear density of the O2 site is preferentially distorted towards the O3 site, as expected from the anisotropic atomic displacement parameters. Again, this is observed as a weak signal in the low threshold nuclear density map, Figure S2. This preferential displacement in combination with the high concentration of oxygen vacancies at the O3 and O2 positions indicates a probable pathway for oxygen vacancy mediated transport between these two positions in the perovskite layer. Conversely, the lack of oxygen vacancies in the O1 position combined with comparatively low atomic displacement indicates that significant oxygen transport does not occur through the O1 sites in the rock-salt layers.

$LaSr_3Co_{1.5}Fe_{1.5}O_{10-\delta}$ (RPn3), Figure 7, has a similar distribution of oxygen vacancies as the RPn2 phase, with the O1 oxygen sites in the rock-salt layer remaining fully occupied at all measured temperatures and the majority of the oxygen vacancies located near the center of the perovskite layers, Figure 8c. Unlike the RPn2 phase however, the vacancies are located on both the O3 and O4 sites, corresponding to the oxygen sites in contact with the center octahedron rather than exclusively in the centermost oxygen site. The overall oxygen occupancy of the RPn3 phase remains higher than that of the RPn2 phase and lower than that of the RPn1. The O3 and O4 sites were best fit with an anisotropic model for atomic displacement, while attempts to fit the O1 and O2 sites with an anisotropic model did not significantly alter the refined χ^2 value, Table 3.

The Fourier nuclear density map, Figure 7, and refined atomic displacement parameters, Table 3, suggests an oxygen transport pathway through the lower occupancy O3 and O4 sites. The O3 site shows anisotropic atomic density in the a-b plane. A possible split in the O4 site can be discerned from the nuclear density at the O4 site which may explain the very large refined anisotropic atomic displacement parameters for the O4 site. Both confirm a large spread in atomic density perpendicular to the B-site in the center of the octahedron. Attempts to refine this oxygen site as a split site did not significantly alter the refined χ^2 value over a single anisotropic position. The high occupancy and relatively low average displacement suggests low transport rate through the O1 sites in the rock-salt layer.

For comparison purposes, the overall oxygen site occupancy between the three structures is shown in Figure 8, and follows the trend RPn2 > RPn3 >> RPn1 at each temperature. This may be expected due to the increasing Sr^{2+} substitution from RPn2 > RPn3 > RPn1. Each individual material also shows the

expected trend of decreasing oxygen stoichiometry with increasing temperature due to reduction of the B-site cations. In all three structures, the density of the oxygen sites located in the B-site layers of the octahedrons are heavily anisotropic in favor of motion tangential to the octahedron, with the oxygen sites located in the A-layers showing a lesser but still present anisotropy with similar preferences. This anisotropy supports the idea of a curved oxygen exchange pathway around the B-site centers of each octahedron[3,4].

A comparison of the direct distances between neighboring oxygen sites for all three materials is shown in Figure 9. The RPn2 has the shortest distance between the most likely sites for oxygen transport, the O2 and O3 sites. Transport distances between O3 and O4 sites in the RPn3 structure were slightly longer at lower temperatures, yet were almost equal at 1070 K. The RPn1 structure had the longest oxygen transport distance, with the distance between neighboring O2 sites shown to be shorter than transport between O1 and O2 sites.

Further comparisons of Co/Fe-O bond lengths as well as comparisons in O-Co/Fe-O bond angles for the three materials are shown in Figures 10 and 11 respectively. The RPn2 phase has significantly more angular distortion in the octahedron centered on the Co/Fe1 site, yet the RPn3 phase had significantly more distortion in Co/Fe-O bond lengths with the Co/Fe1-O3 and Co/Fe2-O3 bond lengths varying significantly from the ideal octahedron with increasing temperature.

The octahedron bordering the rock-salt layer is distorted for all materials by a shift of the O1 site position towards the rock-salt layer and displacement in the Co/Fe1 and neighboring oxygen sites. This is evidenced by a distortion of the O1 site from the La/Sr1 plane, with the O1 site migrating into the rock-salt layer by 11.9%, 9.9%, and 11.1% of the distance between the La/Sr1 planes forming the rock-salt layer, showing that this distortion increases with greater La/Sr ratio.

The Co/Fe1-O3 bond length similarly increases to 2.071 Å and 2.208 Å for the RPn2 and RPn3 phases compared to expected lengths of 1.874 Å and 1.861 Å respectively, assuming the Co/Fe1 position midway between the neighboring La/Sr sites. The corresponding bond length for the RPn1 phase fixed to 2.147 Å by symmetry. The difference between these lengths demonstrates a displacement of the Co/Fe1 site towards the rock-salt layer, likely caused by the available free space in this layer. The equatorial oxygen site O2 is similarly displaced from its ideal site, with an O2-Co/Fe1-O2 angle of 166.77°, and 174.30° for the RPn2 and RPn3 phases with the O2 site located closer to the perovskite. This angle is held constant by symmetry at 180° for the RPn1 phase.

Discussion

The overall oxygen stoichiometry of the three materials follows the trend we may expect with varying La/Sr ratio at a fixed Co/Fe ratio; the oxygen vacancy concentration decreases (oxygen occupancy increases) in the order RPn2 > RPn3 >> RPn1 as Sr/La ratio decreases in the order 9>3>1. Increasing Sr^{2+} substitution for La^{3+} leads to a decrease in overall oxygen site occupancy through oxygen vacancy formation due to charge compensation, holding temperature and pO_2 constant. The temperature dependence of overall oxygen stoichiometry for the RPn1, RPn2, and RPn3 phases, Figure 8, shows the expected trend of decreasing occupancy with increasing temperature at constant pO_2 as the average B-site oxidation state decreases.

We can infer the preferred ion transport pathways in these layered materials through consideration of site occupancy, and observed atomic displacement from the ideal site positions. In general, we find that the vacancies in these materials are primarily located in the perovskite structured layers, confirming the trend identified by several other groups for varying Ruddlesden-Popper materials over a wide range of temperatures[19,30,41-44]. There are almost no oxygen vacancies within the rock-salt layer of any of the Ruddlesden-Popper materials studied, with only the RPn1 phase above 967 K showing any deviation from full occupancy of the O1 site. While this layering of vacancies may be expected to limit ionic conductivity, and thus device performance, similar oxygen vacancy localization is found in the layered perovskites[3,4,45-47] that can provide high performance when employed as SOFC electrode materials.

Oxygen anion transport in the RPn1 structure is limited due to low oxygen vacancy concentrations at both oxygen sites, with the first vacancies forming at 967K. While there are small amounts of oxygen vacancies formed within the O1 site in the rock salt layer for the RPn1 structure, the oxygen transport distances between the O1 and O2 sites range from 2.86 Å – 2.89 Å as the temperature increases from 765 K to 1070 K, slightly longer than the transport distances of 2.72 Å – 2.74 Å between neighboring O2 sites. The transport of oxygen within the RPn1 structure likely utilizes a combination of both the O1-O2-O1 and O2-O2-O2 pathways, as the former utilizes the more vacant O1 site while the latter has reduced transport distances, with the transport likely occurring via a curved pathway[48,49].

There is a correlation between oxygen transport distance and the calculated activation energy for oxygen vacancy transport for a similar composition $La_{2-x}Sr_xCoO_{4-d}$ resulting from molecular dynamics and energy minimization performed by Tealdi et al[50]. The transport pathway of O2-O2-O2 was calculated to have the lowest activation energy for oxygen vacancy migration followed by the O2-O1-O2 pathway and the O1-O1-O1 pathway. This correlation between the direct transport distance and the energy required for motion between the oxygen sites is expected to hold true for materials of similar composition, notably the three Ruddlesden-Popper compositions examined in this work, allowing the measured oxygen transport distances to be utilized as an approximation of the activation energy for oxygen vacancy transport.

The oxygen vacancies in the RPn2 phase are predominantly found at the O3 site in the A-site plane between the two perovskite octahedra. The O3-site oxygen occupancy is as low as 0.56(2) at the highest measurement temperature. Some vacancy formation is observed at the neighboring O2 site in the B-site planes, with a minimum oxygen occupancy of 0.929(7) at the highest measurement temperature. The O1 site in the rock-salt layer is fully occupied under all measurements conditions. This preference for vacancy formation in the A-site plane over the B-site plane is reported in the literature for the related layered-perovskite materials, where oxygen vacancies form almost exclusively in the same plane as either the A or A' cation [3,4,45-47].

If we consider next the direct distances between oxygen sites, transport between neighboring O2 and O3 sites is likely favored due to the relatively short direct distance between these sites, 2.69 Å within error under all measurement conditions. The transport distance between neighboring O2 sites is slightly longer at all measured temperatures, ranging from 2.75 Å to 2.77 Å, suggesting that this alternative hopping pathway may be less favorable, especially considering that such an exchange pathway would not involve the highly vacant O3 site.

The anisotropic atomic displacement of these oxygen sites also suggests a transport pathway between the O2 and O3 sites. There is a significant deviation from the O2 site towards the heavily vacant O3 site, suggesting rapid oxygen exchange between the O2 and O3 sites. The nuclear density on the O2 site is

significantly higher than that on the O3 site, corresponding to differences in oxygen occupancy as shown by the change in color from blue to red in the figure. Unfortunately, the low density on the O3 site makes it difficult to visualize any deviations in density towards the O2 site due to the low signal to noise ratio near this low occupancy site.

The oxygen vacancies in the RPn3 structure are split between the O3 position in an A-site layer and the O2 and O4 positions in the B-site layers of the perovskite. The sites have similar oxygen vacancy concentrations at all measurement conditions. This vacancy spread suggests ion transport primarily between the O2, O3 and O4 sites within the perovskite layers. No vacancies are formed at the O1 site in the rock-salt layer. This vacancy distribution across the RPn3 structure is due to the combination of preferential formation of vacancies within the perovskite layers and the favorable localization of these vacancies in the A-site planes.

The oxygen transport distances are similar between neighboring O4 sites, varying from 2.74 Å – 2.76 Å with increasing temperature, and between O3 and O4 sites, varying from 2.72 Å – 2.69 Å with increasing temperature. The distance between O3 and O4 counterintuitively decreases with increasing temperature. This is due to the increase in lattice parameter from thermal expansion being offset by a shift in the position of the O3 site along the c-axis towards the center of the unit cell. The direct distance between O2 and O3 sites is slightly longer, ranging from 2.78 Å to 2.88 Å, suggesting that this pathway may be less active.

The most significant feature of the nuclear density map for RPn3, Figure 7, is the apparent split in the nuclear density of the O4 site. Despite the insensitivity of the Rietveld quality of fit between a model with split oxygen sites and one without, the presence of such a clear split in the nuclear density map shows that the most likely case is a split in the position of the O4 site, and likely motion between two apparently equivalent positions at the elevated measurement temperature. The O3 and O4 sites shows significant spread in observed density, while the O2 site is more centered on the ideal position. Based on all of these considerations, we suggest that oxygen anions are mobile between the O2, O3, and O4 sites, perhaps with motion between O3 and O4 preferred.

Comparing all of the data, the shortest oxygen transport distances and highest vacancy concentrations are found for the RPn2 materials, followed by RPn3, with RPn1 showing both the longest transport distances and the least vacant oxygen sites. We thus estimate that oxygen transport rates decrease in the order of RPn2 $\gtrsim$ RPn3 >> RPn1. This is likely a function of both structural and composition variation between the materials, resulting in the observed maximum vacancy concentration for the RPn2 phase synthesized in this study. This follows our previously measured trend of surface reaction rate for these materials; RPn2 $\gtrsim$ RPn3 >> RPn1[24]. The surface exchange rate of RPn2 is ~2.0 times greater than RPn3, which is ~9.6 times greater than RPn1.

Ionic conductivity data published by Manthiram, Prado, and Armstrong[16] decreases in the order of RPn3 $\gtrsim$ RPn2 >> RPn1 at 1173K. The trend in ionic conductivity for RPn2 and RPn3 is reversed compared to the trend of surface exchange rates while RPn1 remains relatively inactive. The ionic conductivity of RPn3 is ~1.9 times greater than RPn2, which is ~17.4 times greater than RPn1, in reasonable agreement with our suggested trend of RPn2 $\gtrsim$ RPn3 >> RPn1. Note that the RPn3 and RPn2 compositions are identical to those examined in this study but the measured RPn1 compositions are the end members $Sr_{1.2}La_{0.8}CoO_{4-\delta}$ and $Sr_{1.2}La_{0.8}FeO_{4-\delta}$, suggesting that the crystal structure is the primary factor in determining differences in conductivity between similar compositions. The discrepancy between studies could be due to the difference in measurement temperature, as the surface rates were measured from

623K to 848K, while the bulk ionic conductivity was measured at 1173K. Furthermore, differences in the state of the surface such as preferential segregation of Sr to the surface, surface impurities, and the formation of secondary phases near the surface can greatly impact surface measurements, with these factors changing greatly depending on specific synthesis conditions and sample history[24,51,52]. The difference in oxygen occupancy and transport distances shown through neutron diffraction between the RPn2 and RPn3 phases become smaller as temperature increases, with almost equal values at 1070K, and may reverse at higher temperatures.

There remains a question as to why the three measured Ruddlesden-Popper phases are distorted from the "ideal" structure where the atoms are positioned to form identical cubic perovskite units between ideal rock-salt structures. All three structures show a significant deviation from fully symmetric octahedra, Figures 10 and 11, with significant distortion at the rock-salt / perovskite interface. This displacement, as characterized by the difference in Co/Fe1-O bond lengths, increases with the fraction of La^{3+} on the A-site. SrO forms in the rock salt structure, $Fm\bar{3}m$, with alternating A-site cations and oxygen anions forming the structure, while La_2O_3 forms as trigonal $P\bar{3}m1$. Therefore, higher Sr^{2+} fraction leads to lower distortion within the rock-salt layer. It should be noted that the O1 site shows a much greater spread in nuclear density than would be expected compared to the more vacant and mobile oxygen sites, with a correspondingly greater atomic displacement parameter. The spread in density represents both thermal motion as well as static displacive disorder caused by neighboring cations[53]. This uncertainty in the rock-salt O1 position is in line with similar results for n=1 Ruddlesden-Popper structures[38]. As the O1 position is greatly affected by whether the nearest neighbors are La^{3+} or Sr^{2+} cations, since the oxygen sites displace towards La^{3+} cations.

Increasing density of oxygen vacancies in the center of the perovskite layers of the RPn2 and RPn3 structures leads to a shift in position of the neighboring oxygen sites towards the vacancy rich sites. This can be seen in the change in the O1 - Co/Fe1 - O2 bond angle shown in Figure 11. Increased distortion in the O2 sites towards the center of the perovskite layer can be viewed as an increase in this bond angle. At all temperatures, the RPn2 has a significantly higher O1 - Co/Fe1 - O2 bond angle than the RPn3, although both structures maintain a bond angle above 90°. Similarly, the same trend can be seen by comparing the apical angles of the centermost perovskite octahedra for the RPn2 and RPn3 phases, with angles of 93.57 and 93.06 respectively at 1070 K, where increasing angles correspond to a shift in the equatorial oxygen position towards the center of the unit cell where oxygen vacancy concentrations are highest.

Conclusion

$LaSrCo_{0.5}Fe_{0.5}O_{4-\delta}$ (n=1), $La_{0.3}Sr_{2.7}CoFeO_{7-\delta}$ (n=2), and $LaSr_3Co_{1.5}Fe_{1.5}O_{10-\delta}$ (n=3) Ruddlesden-Popper structures were characterized using neutron powder diffraction under *in-situ* conditions from 765 K-1070 K with a pO_2 of 10^{-1} atm. These structures were characterized by a tetragonal P4/*mmm* space group. The average oxygen occupancy per site varied with increased Sr^{2+} concentration, with values of 0.897, 0.912, and 0.955 corresponding to the RPn2, RPn3, and RPn1 phases respectively. These oxygen vacancies were heavily localized within the perovskite layers of the Ruddlesden-Popper structure, with the rock-salt layers remaining almost completely occupied at all measured temperatures. Analysis of the vacancy localization combined with the atomic displacement parameters suggests oxygen transport pathways through the center of the perovskite layers. Under the assumption of similar mobility per vacancy, these results suggest a trend in oxygen transport of RPn2 $\gtrsim$ RPn3 >> RPn1.

Acknowledgements

A portion of this research at ORNL's Spallation Neutron Source was sponsored by the Scientific User Facilities Division, Office of Basic Energy Sciences, US Department of Energy. Additional support was provided by Lehigh University. Mazin Tamimi is a sponsored student supported by the Saudi Arabian Oil Company, Saudi Aramco.

Figure 1. Ruddlesden-Popper unit cells for a) n = 1 (RPn1), b) n = 2 (RPn2), and c) n = 3 (RPn3) structures. Note that these structures are derived from Rietveld refinement of the neutron diffraction data collected at 1070 K and pO_2 of 0.1 atm. Numbers in blue denote refined oxygen site occupancy at these conditions.

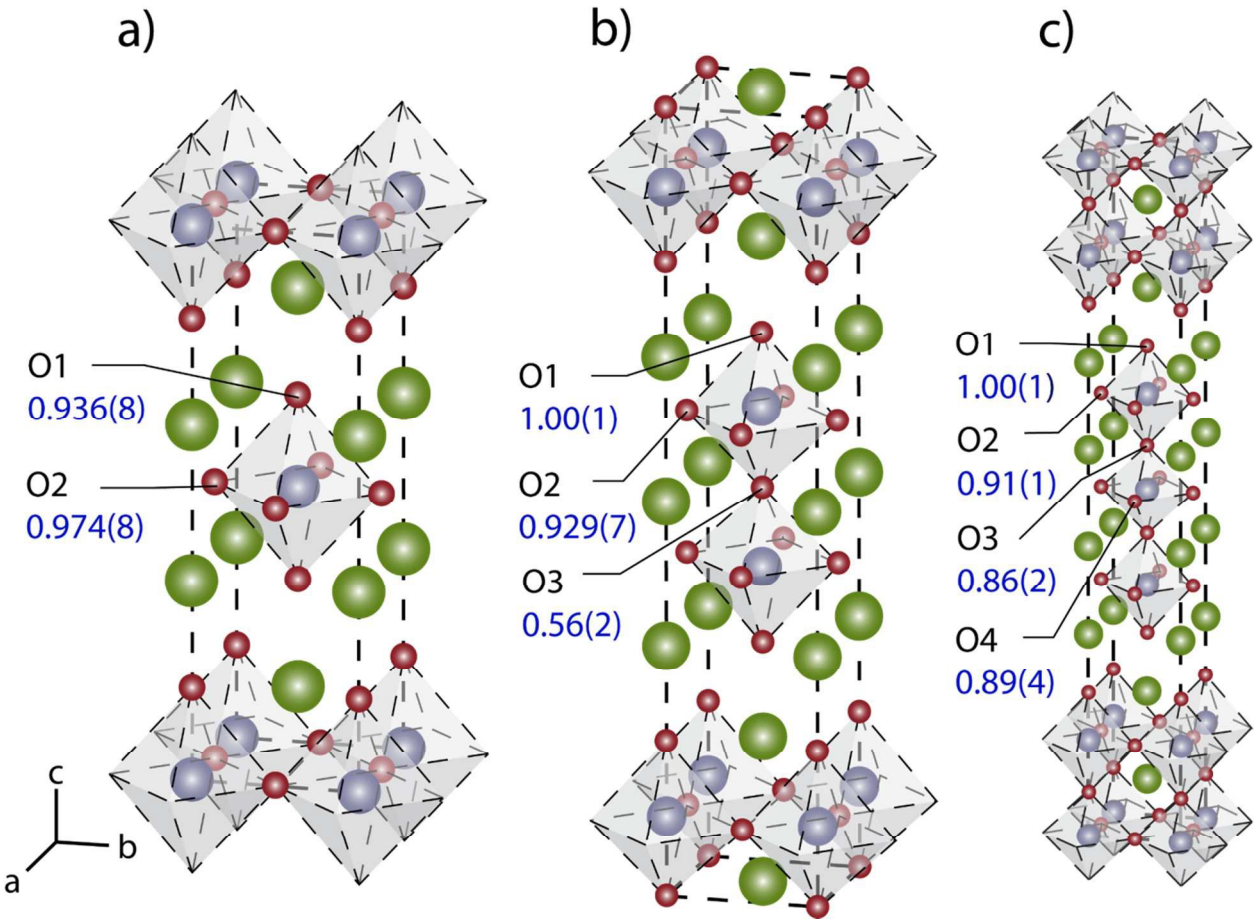

Figure 2. Representative data from neutron diffraction at 1070 K with a pO_2 of .1 atm for a) $LaSrCo_{0.5}Fe_{0.5}O_{4-\delta}$ (RPn1), b) $La_{0.3}Sr_{2.7}CoFeO_{7-\delta}$ (RPn2), and c) $LaSr_3Co_{1.5}Fe_{1.5}O_{10-\delta}$ (RPn3) samples. All three materials exhibited I4/mmm space group structures. A perovskite ($Pm\bar{3}m$) impurity was identified in each sample, with the primary diffraction peak marked by an asterisk below. Measured data (black dots), calculated diffraction pattern (top red line), difference pattern (bottom blue line), and expected peak positions are shown.

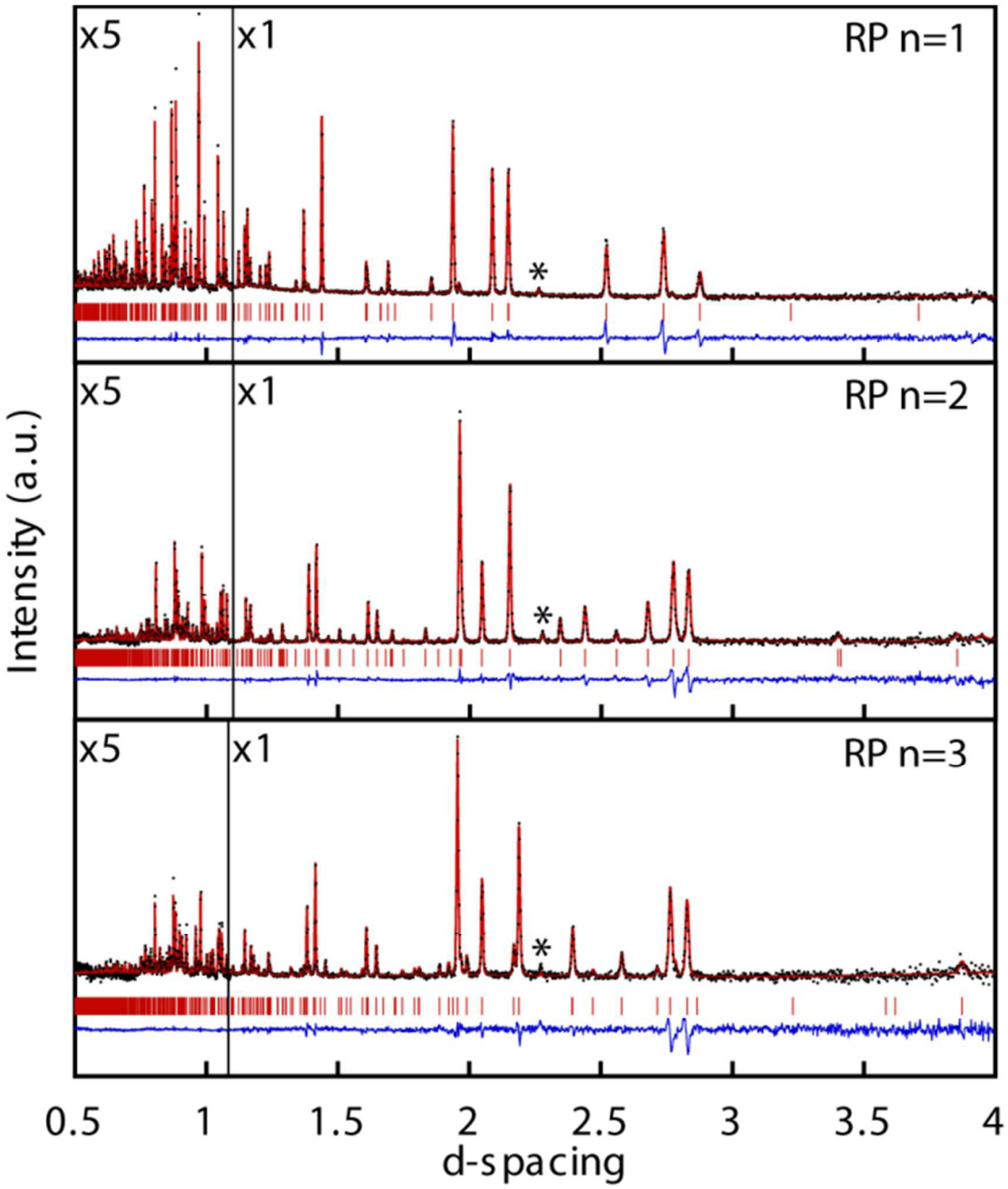

Figure 3. *a* lattice parameter for RPn1 (Red circle), RPn2 (Blue inverted triangle), RPn3 (Green square).

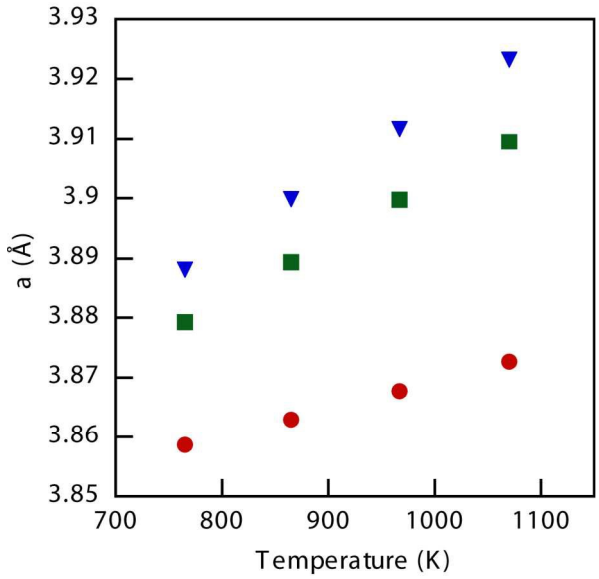

Figure 4: *c* lattice parameter for RPn1 (Red circle), RPn2 (Blue inverted triangle), RPn3 (Green square).

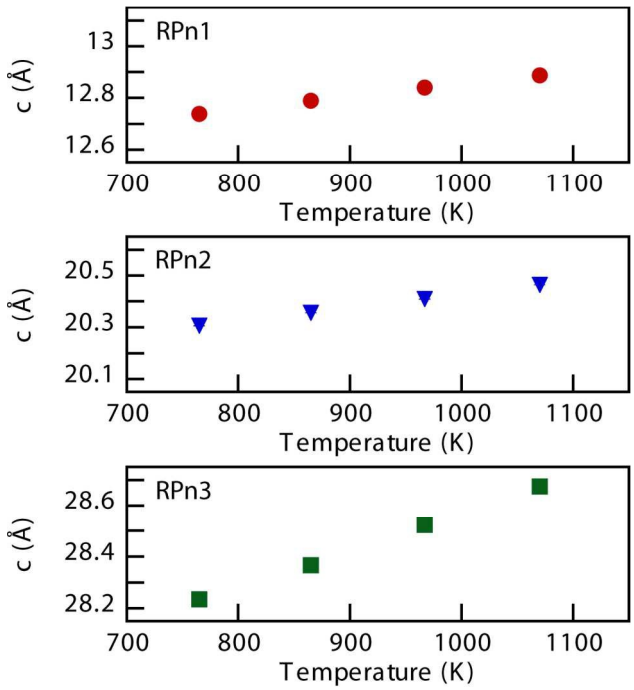

Figure 5. Fourier observed nuclear density diagram at 1070 K with a pO_2 of .1 atm for $LaSrCo_{0.5}Fe_{0.5}O_{4-\delta}$ (RPn1). The progression of color from blue to green to red denotes an increase in the observed nuclear density, showing the probable positions for the atoms. Slices of the observed nuclear density along several different planes are shown for the different oxygen sites.

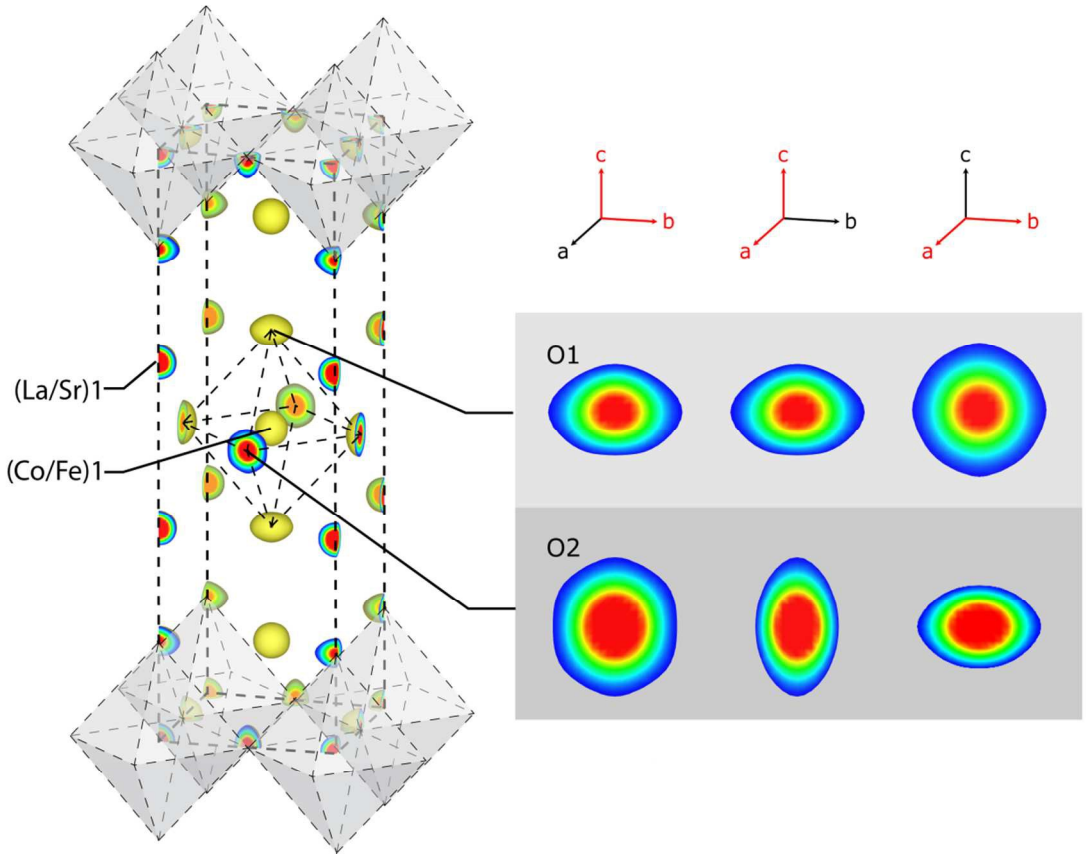

Figure 6. Fourier observed nuclear density diagram at 1070 K with a pO_2 of .1 atm for $La_{0.3}Sr_{2.7}CoFeO_{7-\delta}$ (RPn2). The progression of color from blue to green to red denotes an increase in the observed nuclear density, showing the probable positions for the atoms. Slices of the observed nuclear density along several different planes are shown for the different oxygen sites.

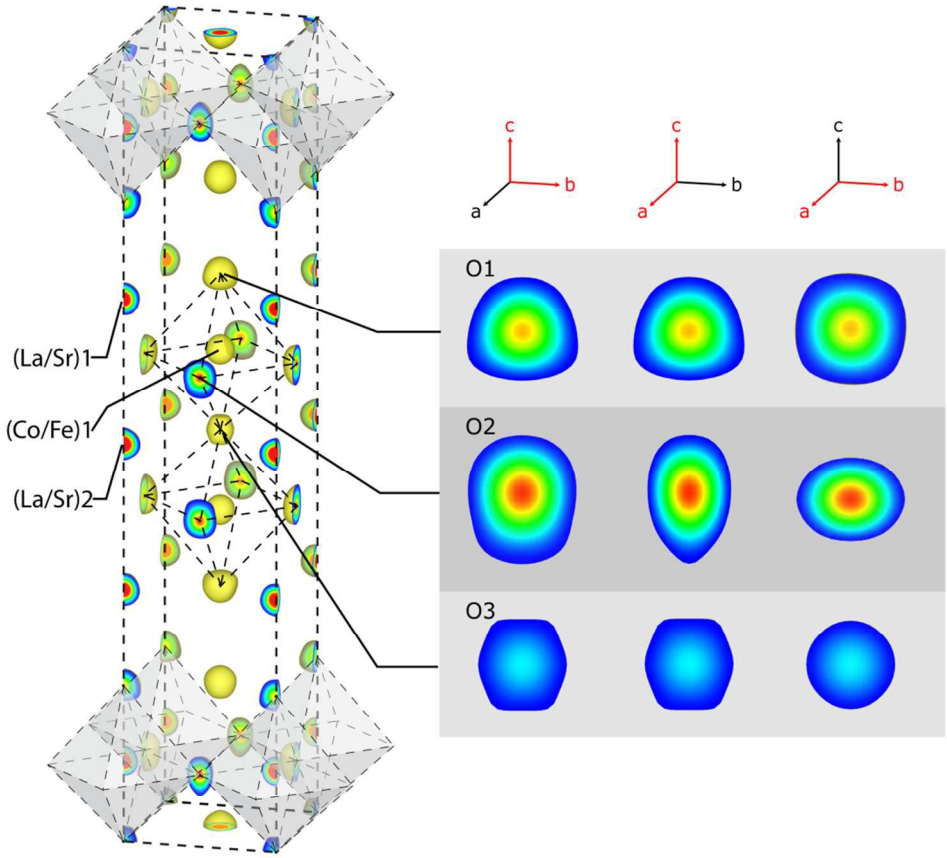

Figure 7. Fourier observed nuclear density diagram at 1070 K with a pO_2 of .1 atm $LaSr_3Co_{1.5}Fe_{1.5}O_{10-\delta}$ (RPn3). The progression of color from blue to green to red denotes an increase in the observed nuclear density, showing the probable positions for the atoms. Slices of the observed nuclear density along several different planes are shown for the different oxygen sites.

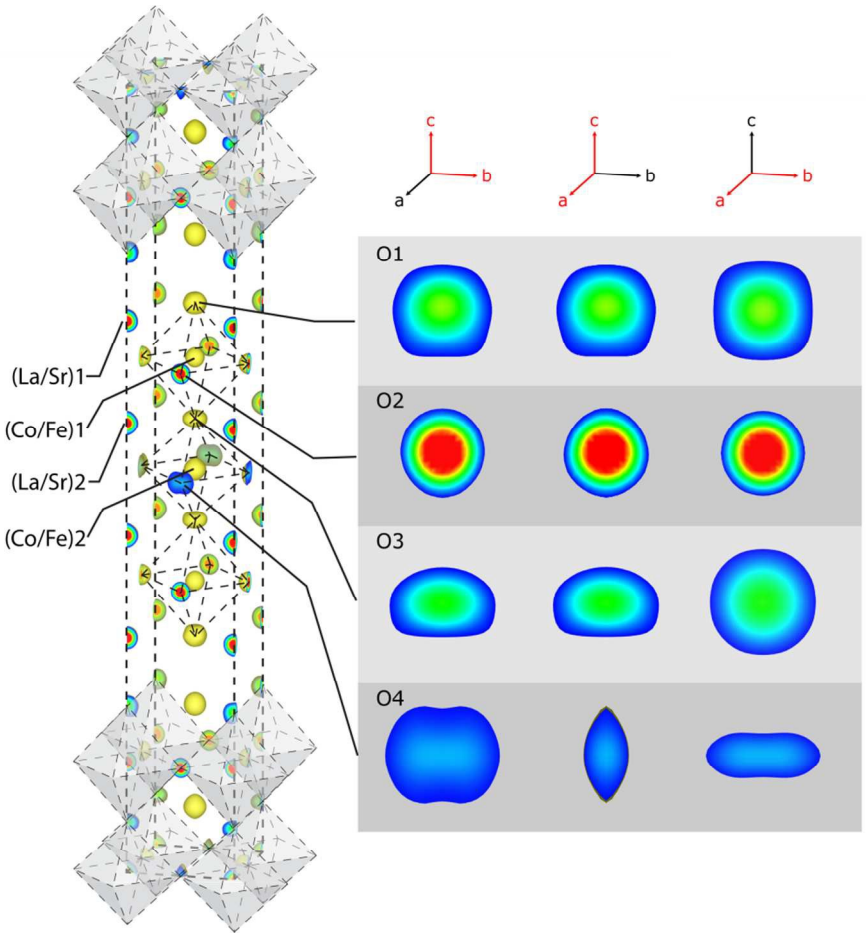

Figure 8. Oxygen site occupancies for a)RPn1, b)RPn2, and c)RPn3 phases. Sites displayed include O1 (blue diamond), O2 (red square), O3 (green inverted triangle), and O4 (gold triangle). Overall oxygen occupancy at each temperature is denoted by black circles connected by the dashed line.

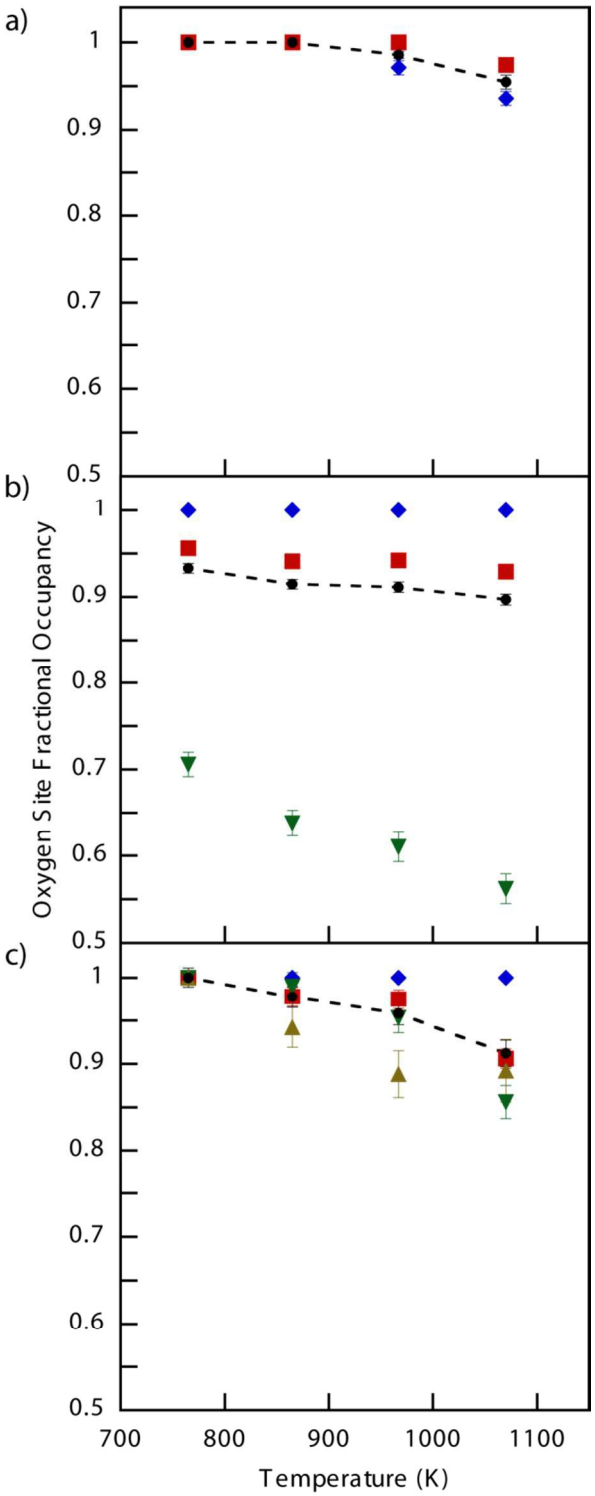

Figure 9. Direct oxygen transport distances between nearest oxygen sites: RPn1 O2 - O2 (Red closed circle), RPn1 O1 - O2 (Red triangle), RPn2 O2 - O2 (Blue open square), RPn2 O2 - O3 (Blue inverted triangle), RPn3 O2 - O3 (Green open circle), RPn3 O3 - O4 (Green closed square), RPn3 O4 - O4 (Green diamond).

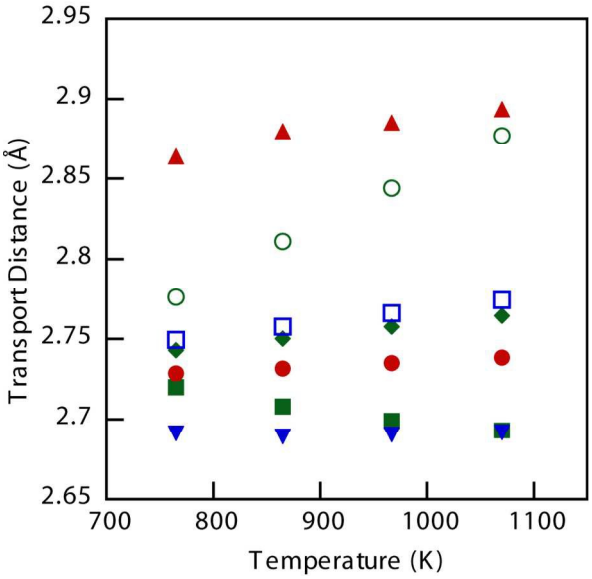

Figure 10. Co/Fe - O bond lengths for: a) RPn1 structure Co/Fe1 - O1 (Blue Diamond), Co/Fe1 - O2 (Red square) b) RPn2 structure Co/Fe1 - O1 (Blue Diamond), Co/Fe1 - O2 (Red square), Co/Fe1 - O3 (Green inverted triangle) c) RPn3 structure Co/Fe1 - O1 (Blue Diamond), Co/Fe1 - O2 (Red square), Co/Fe1 - O3 (Green inverted triangle), Co/Fe2 - O3 (Gold triangle), Co/Fe2 - O4 (Black circle, located under Co/Fe1 - O2 red squares).

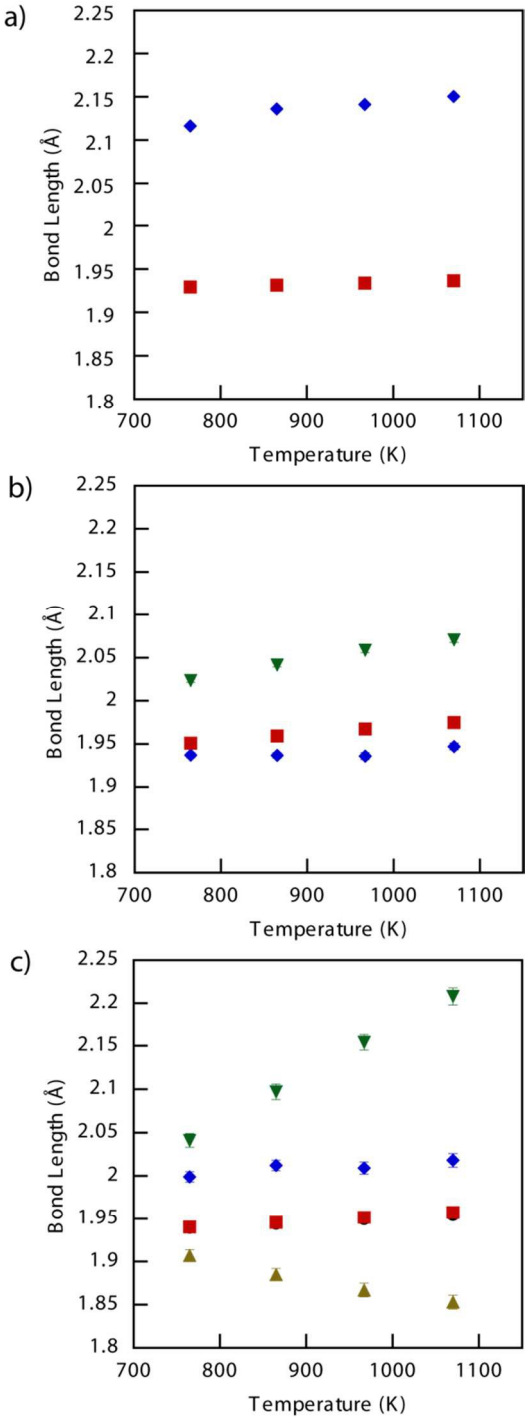

Figure 11. Bond angle of O1 - Co/Fe1 - O2 bond for RPn2 (Blue inverted triangle) and RPn3 (Green square) structures. Increased angle above 90^{o} corresponds to a distortion of the O2 site towards the perovskite layers compared to an ideal octahedron.

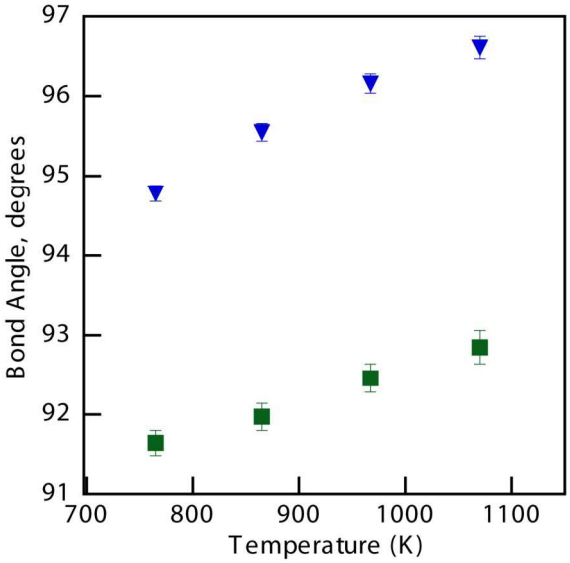

Table 1: Tetragonal space group I4/mmm, Rietveld fit parameters for RPn1 structure at 1070 K with sites:

RPn1: La/Sr1: 4e (0,0,Z), Co/Fe1: 2a (0,0,0), O1: 4e (0,0,Z), O2: 4c (0.5,0,0)

RPn1 I4/mmm 1070 K

a,b (Å)	3.873(1)		χ^2	4.060	
c (Å)	12.887(1)		R_P %	0.0974	
V (Å^3)	193.58(1)		wR_P %	0.0392	
ρ_c (g/cm^3)	5.929				
	Atomic displacement parameters (Å^2)*100				Fractional
	U_{11}/U_{iso}	U_{22}	U_{33}	Z	Occupancy
La/Sr1	2.16(3)			0.359(1)	
Co/Fe1	1.71(4)				
O1	3.88(7)	3.88(7)	1.8(1)	0.167(1)	0.936(8)
O2	0.97(7)	2.9(1)	3.7(1)		0.974(8)

Table 2: Tetragonal space group I4/mmm, Rietveld fit parameters for RPn2 structure at 1070 K with sites:

RPn2: La/Sr1: 4e (0,0,Z), La/Sr2: 2b (0,0,0.5), Co/Fe1: 4e (0,0,Z), O1: 4e (0,0,Z), O2: 8g (0,0.5,Z), O3: 2a (0,0,0)

RPn2 I4/mmm 1070 K

a,b (Å)	3.923(1)	χ^2	4.036
c (Å)	20.464(1)	R_P %	0.1499
V (Å^3)	314.97(1)	wR_P %	0.0596
ρ_c (g/cm^3)	5.203		

	Atomic displacement parameters (Å^2)*100				Fractional
	U_{11}/U_{iso}	U_{22}	U_{33}	Z	Occupancy
La/Sr1	3.20(7)			0.317(1)	
La/Sr2	2.80(9)				
Co/Fe1	2.08(5)			0.101(1)	
O1	4.13(8)			0.196(1)	1.0
O2	3.9(1)	2.0(1)	5.0(2)	0.090(1)	0.929(7)
O3	5.5(4)				0.56(2)

Table 3: Tetragonal space group I4/mmm, Rietveld fit parameters RPn3 structure at 1070 K with sites:

RPn3: La/Sr1: 4e(0,0,Z), La/Sr2: 4e (0,0,Z), Co/Fe1: 4e (0,0,Z), Co/Fe2: 2a (0,0,0), O1: 4e (0,0,Z), O2: 8g (0,0.5,Z), O3: 4e (0,0,Z), O4: 4c (0,0.5,0)

RPn3 I4/mmm 1070 K

a,b (Å)	3.909(1)	χ^2	2.381
c (Å)	28.675(1)	R_P%	0.1431
V (Å^3)	438.29(2)	wR_P%	0.0541
ρ_c (g/cm^3)	5.455		

	Atomic displacement parameters (Å^2)*100				Fractional
	U_{11}/U_{iso}	U_{22}	U_{33}	Z	Occupancy
La/Sr1	3.3(1)			0.2011(2)	
La/Sr2	3.5(1)			0.0713(2)	
Co/Fe1	2.0(1)			0.1416(1)	
Co/Fe2	3.7(2)				
O1	4.7(2)			0.2120(2)	1
O2	2.3(1)			0.1382(2)	0.91(1)
O3	6.0(4)	6.0(4)	3.1(4)	0.0646(3)	0.86(2)
O4	18.1(2)	1.8(6)	21(2)		0.89(4)

Reference List

[1] S.P. Simner, J.F. Bonnett, N.L. Canfield, K.D. Meinhardt, J.P. Shelton, V.L. Sprenkle, J.W. Stevenson, *J. Power Sources.* 2003, 113, 1-10.

[2] A.J. Jacobson, *Chem. Mater.* 2010, 22, 660-674.

[3] R.A. Cox-Galhotra, A. Huq, J.P. Hodges, C. Yu, X. Wang, W. Gong, A.J. Jacobson, S. McIntosh, *Solid State Ionics.* 2013, 249–250, 34-40.

[4] R. Cox-Galhotra, A. Huq, J.P. Hodges, J. Kim, C. Yu, X. Wang, A.J. Jacobson, S. McIntosh, *J. Mater. Chem. A.* 2013, 1, 3091-3100.

[5] H.J.M. Bouwmeester, C. Song, J. Zhu, J. Yi, M. van Sint Annaland, B.A. Boukamp, *Physical Chemistry Chemical Physics.* 2009, 9640-9643.

[6] D.N. Mueller, R.A. De Souza, H. Yoo, M. Martin, *Chem. Mater.* 2012, 24, 269-274.

[7] S. McIntosh, J.F. Vente, W.G. Haije, D.H.A. Blank, H.J.M. Bouwmeester, *Solid State Ionics.* 2006, 177, 1737-1742.

[8] A. Tarancon, M. Burriel, J. Santiso, S.J. Skinner, J.A. Kilner, *J. Mater. Chem.* 2010, 20, 3799-3813.

[9] G. Amow, I.J. Davidson, S.J. Skinner, *Solid State Ionics.* 2006, 177, 1205-1210.

[10] V.V. Kharton, A.P. Viskup, A.V. Kovalevsky, E.N. Naumovich, F.M.B. Marques, *Solid State Ionics.* 2001, 143, 337-353.

[11] V. Kharton V., A. Viskup P., E. Naumovich N., F. Marques M.B., *J. Mater. Chem.* 1999, 9, 2623-2629.

[12] A.V. Kovalevsky, V.V. Kharton, A.A. Yaremchenko, Y.V. Pivak, E.V. Tsipis, S.O. Yakovlev, A.A. Markov, E.N. Naumovich, J.R. Frade, *Journal of Electroceramics.* 2007, 18, 205-218.

[13] J.M. Bassat, P. Odier, A. Villesuzanne, C. Marin, M. Pouchard, *Solid State Ionics.* 2004, 167, 341-347.

[14] S.J. Skinner, J.A. Kilner, *Solid State Ionics.* 2000, 135, 709-712.

[15] J.A. Kilner, C.K.M. Shaw, *Solid State Ionics.* 2002, 154–155, 523-527.

[16] A. Manthiram, F. Prado, T. Armstrong, *Solid State Ionics.* 2002, 152–153, 647-655.

[17] I. Kagomiya, K. Jimbo, K. Kakimoto, M. Nakayama, O. Masson, *Phys. Chem. Chem. Phys.* 2014, 16, 10875-10882.

[18] A.A. Markov, M.V. Patrakeev, V.V. Kharton, Y.V. Pivak, I.A. Leonidov, V.L. Kozhevnikov, *Chem. Mater.* 2007, 19, 3980-3987.

[19] F. Prado, T. Armstrong, A. Caneiro, A. Manthiram, *Journal of The Electrochemical Society.* 2001, 148, J7-J14.

[20] Y.A. Shilova, M.V. Patrakeev, E.B. Mitberg, I.A. Leonidov, V.L. Kozhevnikov, K.R. Poeppelmeier, *Journal of Solid State Chemistry.* 2002, 168, 275-283.

[21] A.C. Tomkiewicz, M. Meloni, S. McIntosh, *Solid State Ionics.* 2014, 260, 55-59.

[22] S. McIntosh, Oxygen Anion Transport in Solid Oxides, in: G. Kreysa, K. Ota, R. Savinell (Eds.), Springer New York, 2014, pp. 1461-1475.

[23] S. McIntosh, J.F. Vente, W.G. Haije, D.H.A. Blank, H.J.M. Bouwmeester, *Solid State Ionics.* 2006, 177, 833-842.

[24] A.C. Tomkiewicz, M.A. Tamimi, A. Huq, S. McIntosh, *Faraday Discuss.* 2015,.

[25] M.A. Tamimi, S. McIntosh, *J. Mater. Chem. A.* 2014, 2, 6015-6026.

[26] S. McIntosh, J.F. Vente, W.G. Haije, D.H.A. Blank, H.J.M. Bouwmeester, *Chem. Mater.* 2006, 18, 2187-2193.

[27] A.C. Tomkiewicz, M.A. Tamimi, A. Huq, S. McIntosh, *Solid State Ionics.* 2013, 253, 27-31.

[28] M.A. Tamimi, A.C. Tomkiewicz, A. Huq, S. McIntosh, *J. Mater. Chem. A.* 2014, 2, 18838-18847.

[29] E. Bonturim, V. Mazzocchi, C. Parente, J. Mestnik-Filho, N. de Lima, E. Seo, *J. Radioanal. Nucl.* 2015, 1-5.

[30] T. Armstrong, F. Prado, A. Manthiram, *Solid State Ionics.* 2001, 140, 89-96.

[31] I. Sharma, D. Singh, *Bull. Mater. Sci.* 1998, 21, 363-374.

[32] R. van Doorn H.E., H. Kruidhof, A. Nijmeijer, L. Winnubst, A. Burggraaf J., *J. Mater. Chem.* 1998, 8, 2109-2112.

[33] Y.S. Touloukian, R.K. Kriby, R.E. Taylor, P.D. Desai, Thermophysical Properties of Matter, Purdue Research Foundation, 1977.

[34] H.M. Rietveld, *J. Appl. Crystallog.* 1969, 2, 65-71.

[35] A.C. Larson, R.B. von Dreele, *Los Alamos National Laboratory: Los Alamos, New Mexico.* 2004,.

[36] E. B. H. Toby, *J. Appl. Cryst.* 2001,34, 210-213.

[37] R.B. Von Dreele, J.D. Jorgensen, C.G. Windsor, *Journal of Applied Crystallography.* 1982, 15, 581-589.

[38] C. Chatzichristodoulou, B.C. Hauback, P.V. Hendriksen, *Journal of Solid State Chemistry.* 2013, 201, 164-171.

[39] M. Bahout, F. Tonus, C. Prestipino, D. Pelloquin, T. Hansen, E. Fonda, P.D. Battle, *J. Mater. Chem.* 2012, 22, 10560-10570.

[40] C. Chatzichristodoulou, C. Schönbeck, A. Hagen, P.V. Hendriksen, *Solid State Ionics.* 2013, 232, 68-79.

[41] G.N. Mazo, S.M. Kazakov, L.M. Kolchina, S.Y. Istomin, E.V. Antipov, N.V. Lyskov, M.Z. Galin, L.S. Leonova, Y.S. Fedotov, S.I. Bredikhin, Y. Liu, G. Svensson, Z. Shen, *Solid State Ionics.* 2014, 257, 67-74.

[42] S.E. Dann, M.T. Weller, D.B. Currie, *Journal of Solid State Chemistry.* 1992, 97, 179-185.

[43] F. Prado, L. Mogni, G.J. Cuello, A. Caneiro, *Solid State Ionics.* 2007, 178, 77-82.

[44] J.Y. Lee, J.S. Swinnea, H. Steinfink, W.M. Reiff, S. Pei, J.D. Jorgensen, *Journal of Solid State Chemistry.* 1993, 103, 1-15.

[45] J.F. Mitchell, J. Burley, S. Short, *J. Appl. Phys.* 2003, 93, 7364-7366.

[46] D. Khalyavin, O. Prokhnenko, N. St\u\sser, V. Sikolenko, V. Efimov, A. Salak, A. Yaremchenko, V. Kharton, *Phys.Rev.B.* 2008, 77, 174417.

[47] L.S. Lobanovsky, I.O. Troyanchuk, H. Szymczak, O. Prokhnenko, *Journal of Experimental and Theoretical Physics.* 2006, 103, 740-746.

[48] M. Saiful Islam, *J. Mater. Chem.* 2000, 10, 1027-1038.

[49] M. Cherry, M.S. Islam, C.R.A. Catlow, *Journal of Solid State Chemistry.* 1995, 118, 125-132.

[50] C. Tealdi, C. Ferrara, P. Mustarelli, M.S. Islam, *J. Mater. Chem.* 2012, 22, 8969-8975.

[51] M. Kubicek, A. Limbeck, T. Frömling, H. Hutter, J. Fleig, *Journal of The Electrochemical Society.* 2011, 158, B727-B734.

[52] J. Druce, H. Tellez, M. Burriel, M.D. Sharp, L.J. Fawcett, S.N. Cook, D.S. McPhail, T. Ishihara, H.H. Brongersma, J.A. Kilner, *Energy Environ. Sci.* 2014, 7, 3593-3599.

[53] J.D. Dunitz, V. Schomaker, K.N. Trueblood, *J. Phys. Chem.* 1988, 92, 856-867.

Table of Contents

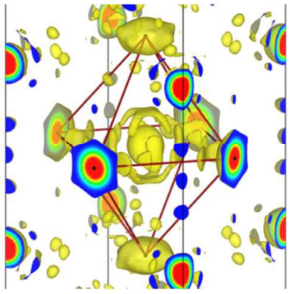

In-situ neutron diffraction techniques were utilized to provide detailed information about the crystal structure of n=1, n=2, and n=3 Ruddlesden-Popper structures focusing on the oxygen transport pathways created by localization of oxygen vacancies. Results are compared to previously measured ionic conductivity and surface oxygen exchange rates.